A Novel Technique for 4-Dimensional Atmospheric and Oceanographic Irradiance Measurements Using 3-D Spatial Filtering

Contract No. N00014-94-C-0099

Period of Performance: 04/14/94 to 09/30/94

Final Report

Reporting Period: 04/14/94 to 09/30/94

Presented to:

Office of Naval Research
Ballston Tower One
800 North Quincy Street
Arlington, VA 22217-5660

Scientific Officer:
Steve Ackleson

Presented by:

Physical Optics Corporation
Research and Development Division
20600 Gramercy Place, Suite 103
Torrance, California 90501

September 1994

SUMMARY

In this project, POC advanced and optimized a spatial filtering technique for measuring irradiance spatial density. The key component of the novel technique is a pixel filter placed at the image focal plane. The pixel filter design includes a wavefront-matched filter, a microlens, and a point detector. The pixel filter allows the light from the in-focus volume to pass, suppressing the light from out-of-focus areas.

Three objectives were established for the Phase I project and its Option Task. This report does not concern the Option Task since that task has not been performed yet. The objectives were:

Objective 1 Numerically analyze and characterize the properties of an imaging system using the proposed 3-D spatial filtering technique, and determine optimal system design parameters

Objective 2 Construct a single pixel filter, and experimentally demonstrate the proof-of-concept of the technique

Objective 3 Identify work to be performed in Phase II of this research.

POC Physical Optics Corporation

October 5, 1994

Scientific Officer
Attn: Steve Ackleson
Office of Naval Research, Code N00014
800 North Quincy St., One Ballston Tower 1
Arlington, VA 22217-5660

Reference: Contract No. N00014-94-C-0099
"A Novel Technique for 4-Dimensional Atmospheric & Oceanographic Irradiance Measurements Using 3-D Spatial Filtering"

Dear Mr. Ackleson:

Enclosed is the Final Report, Final DD Form 882 and DD Form 250 Invoice for the above referenced project. Upon your approval of the DD250 please return one signed copy to me in the envelope provided.

Please feel free to contact me at 310/320-3088 if you have any questions or require additional information.

Sincerely,

Georgia Burnett
Contract Administrator

GB/pl
Enclosure: (1,3)
cc: ACO (1)
Code 2627 (1)
DTIC (2)
Ref: 3267

20600 Gramercy Place, Building 100, Torrance, California 90501 • (310) 320-3088 • FAX (310) 320-4667

1.0 MODELING THE IMAGING SYSTEM

This im: system can be described in terms of two diffractions. The geometry of the system is represented in Figure 1.

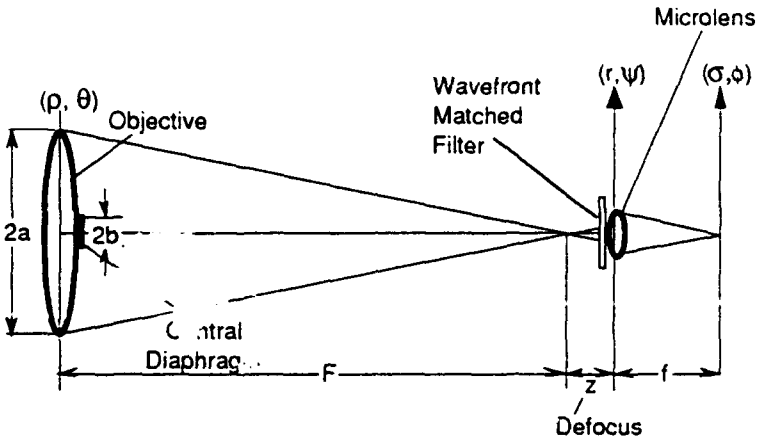

Figure 1
Geometry of the double diffraction system.

Suppose that a, b, c, and e are the radii of the objective lens, the central diaphragm, the microlenses and the pinholes, respectively; F and f are the imaging distance and the focal length of microlenses, respectively; z is the defocus distance. Finally, (ρ,θ), (r,ψ), and (σ,ϕ) are polar coordinate systems in the objective lens plane, microlens plane, and the output image plane, respectively. Let us define the following normalized coordinates:

$$u = \frac{2\pi}{\lambda}\left(\frac{a}{F}\right)^2 z \tag{1}$$

and

$$v = \frac{2\pi}{\lambda}\left(\frac{a}{F}\right) r \quad . \tag{2}$$

The optical field on the microlens array plane can be calculated by

$$W(u,v) = \int_{b/a}^{1} J_0(v\cdot\rho)\exp\left(ju\frac{\rho^2}{2}\right)\rho d\rho, \tag{3}$$

where $J_0(x)$ is the zero order Bessel function. This is the optical field generated by a point source located at the axial point of the object plane.

In order to simplify the calculations, we first calculated the defocus response for a point source array on the object plane. The point source separation is equal to the diameter of the microlens, c. Further, we assumed that the point source array is arranged in circular symmetry as show in Figure 2. The M-th ring of point sources is on a circle with a radius equal to Mc. All point sources contribute energy to the pinhole on the axis shown in Figure 1. We sum up the energy from all point sources to calculate the defocus response.

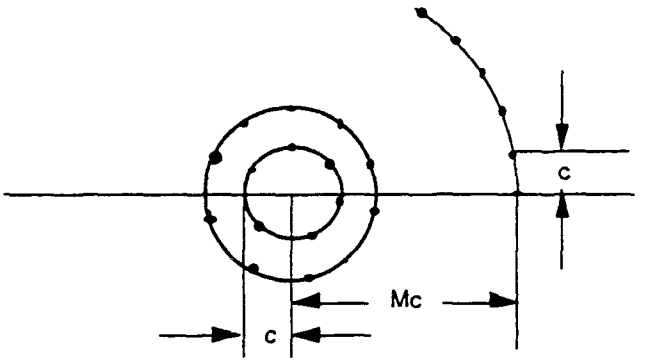

Figure 2
A point source array arranged in circular symmetry.

For the sake of convenient calculation, we calculated the energy summation in another way. Rather than assuming a point source array and single pixel filter, we equivalently used a pixel filter array and a single point source for the numerical calculation. Thus, we have a microlens array with a pinhole array on the focal plane of the microlens array. The microlenses are arranged in the same way as the point sources shown in Figure 2. We calculated the field diffracted onto each microlens by the imaging lens, then calculated the field on the corresponding pinholes, and finally, summed the energy on all pinholes.

It is convenient to introduce a local coordinate system for each microlens and pinhole as shown in Figure 3.

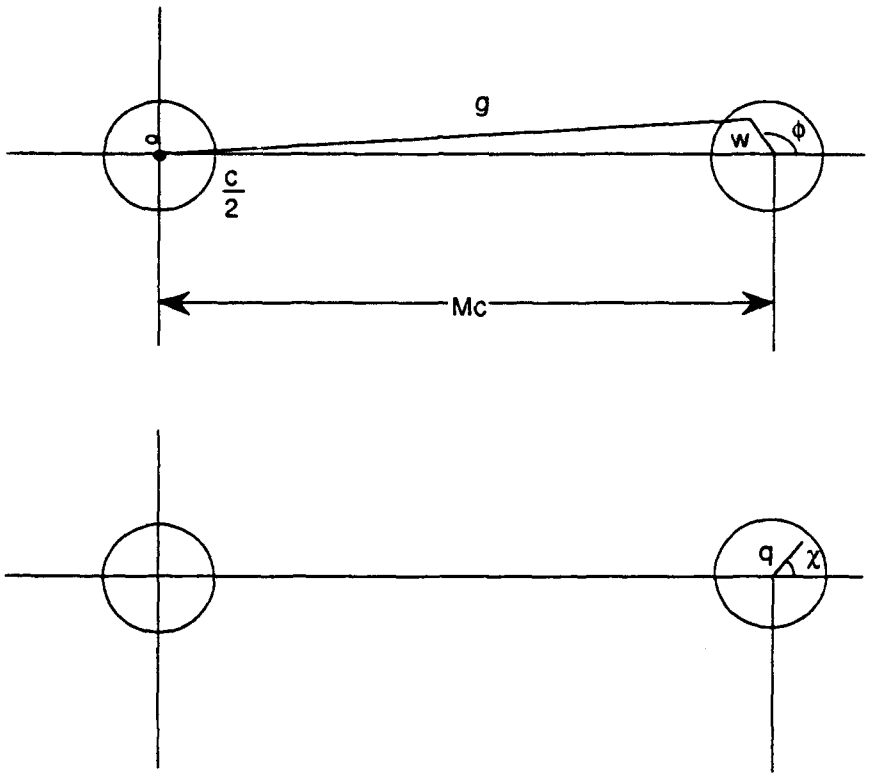

Figure 3
Local coordinate systems (w,ϕ) for the microlens plane and (q,χ) for the pinhole plane.

The fields on the M-th microlens can be expressed by Eq. (3), where $\frac{2\pi}{\lambda}\left(\frac{a}{F}\right)g$ is used for v in Eq. (2), and g is given by

$$g = \sqrt{(2Mc + w\cos\phi)^2 + (w\sin\phi)^2} \quad . \tag{4}$$

The field on the pinhole plane diffracted by the M-th microlens can be expressed by a Fourier transform in the polar coordinate system

$$G_M(u, q, \chi) = \int_0^{2\pi} d\phi \int_0^{C/2} W\left(u, \frac{2\pi}{\lambda}\left(\frac{a}{F}\right)g\right) \exp\left[-j\frac{(2\pi)^3}{\lambda}\left(\frac{a}{F}\right)^2 wq\cos(\phi - \chi)\right] \cdot wdw \quad . \tag{5}$$

To simplify the calculation, the field on the pinhole is considered to be uniform so that only the field at the center of the pinhole (that is, q = 0 in Eq. (5)) need be calculated. Thus, we can drop both q and χ in Eq. (5) so that

$$G_M(u) = \int_0^{2\pi} d\phi \int_0^C W\left(u, \frac{2\pi}{\lambda}\left(\frac{a}{F}\right)g\right) \, wdw \quad . \tag{6}$$

To sum up the energy at all pinholes, we only need to calculate the field intensity in the pinholes in one radial direction.

The total intensity from the pinholes on the M-th ring is estimated by multiplying the equivalent number of microlenses in a given ring by the intensity at the M-th pinhole. The equivalent number of microlenses on the M-th ring is given by

$$2\pi M + \delta(M) \quad , \tag{7}$$

where

$$\delta(M) = \begin{cases} 1, & \text{for } M = 0, \\ 0, & \text{for } M \neq 0. \end{cases} \tag{8}$$

Thus, the energy summation can be expressed

$$I(u) = \sum_{M=0}^{M_{max}} \left|G_M(u)\right|^2 (2\pi M + \delta(M)) \quad . \tag{9}$$

Notice that I(u) is a function of u, the normalized defocus distance (see Eq. (1)), representing the defocus response of the imaging system. If I(u) is not dependent on u, it means that the system has no depth discrimination capability. If I(u) is a function with a strong peak at u = 0, the system has strong depth discrimination capability. In the following sections, we use the formulas developed above to evaluate the depth discrimination capabilities for various situations.

2.0 OPTIMIZED DESIGN OF THE PIXEL FILTER

Figure 5(a) shows the diffracted field on the microlens plane, according to Eq. (3) with the central obstruction ratio b/a = 0.5. It consists of a central spot and a few rings. If the microlens diameter is greater than the central spot size (Airy spot size), a π-phase wavefront matched filter is required to correct the negative phase of the pattern. The phase distribution of the filter is shown in Figure 5(b). Figure 5(c) shows the structure of the pixel filter.

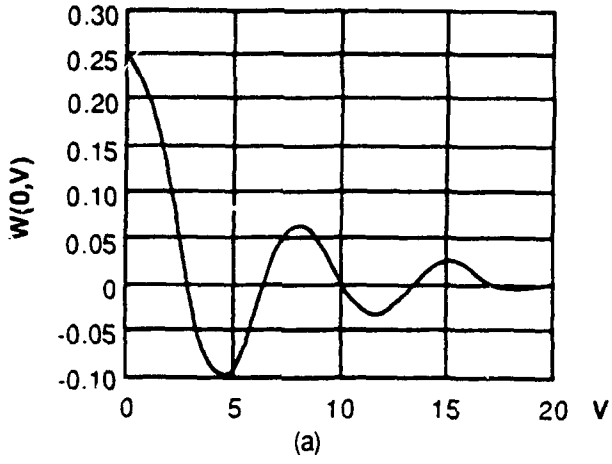

(a)

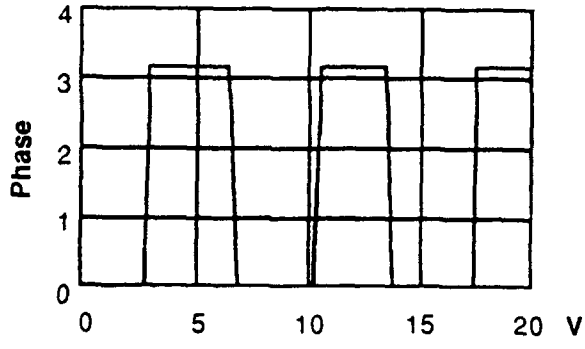

(b)

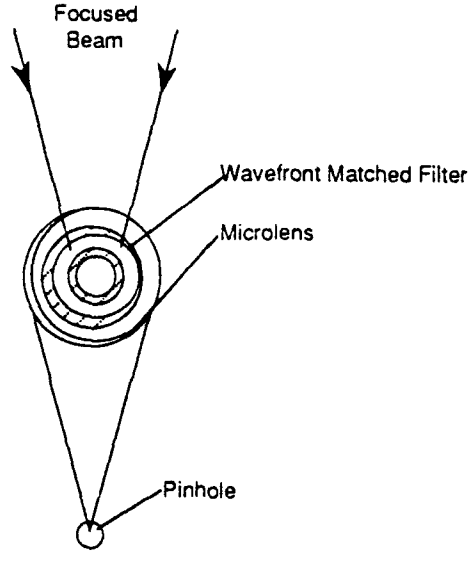

(c)

Figure 5
(a) Field amplitude distribution on the wavefront matched filter, (b) phase distribution of the wavefront matched filter, and (c) structure of a pixel filter.

A larger microlens would yield a higher discrimination ratio, but would require more space and a matched filter with many π-phase rings. We performed numerical simulations to find an optimized tradeoff between the size of the microlens and the discrimination ratio. Figure 6 shows the defocus response for pixel filters with a microlens size of ten times that of the Airy spot. The matched filter requires five rings, as illustrated in Figure 7. The effect of the rings away from the center is relatively small. In the selected tradeoff, only two rings are required. The resulting defocus response is shown in Figure 8.

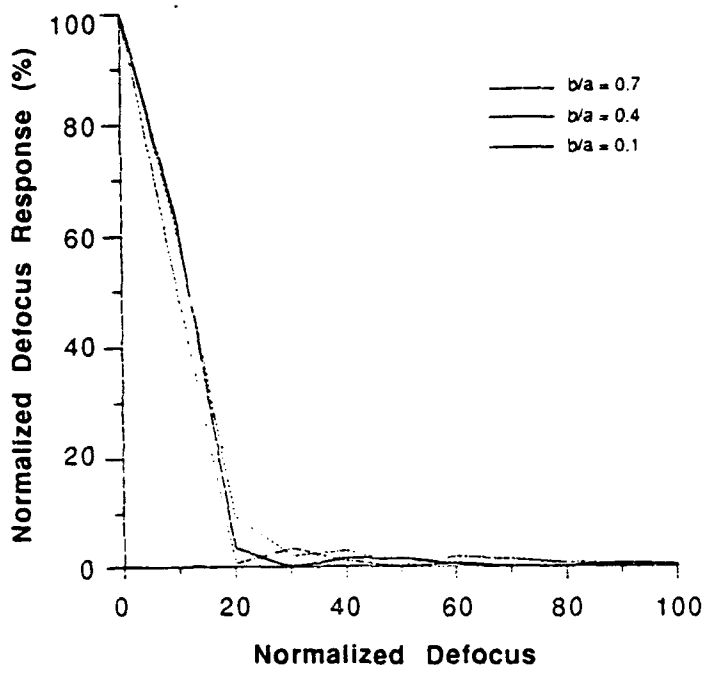

Figure 6
Defocus response for various values of central obstruction ratio b/a
(microlens size is equal to ten times Airy spot size).

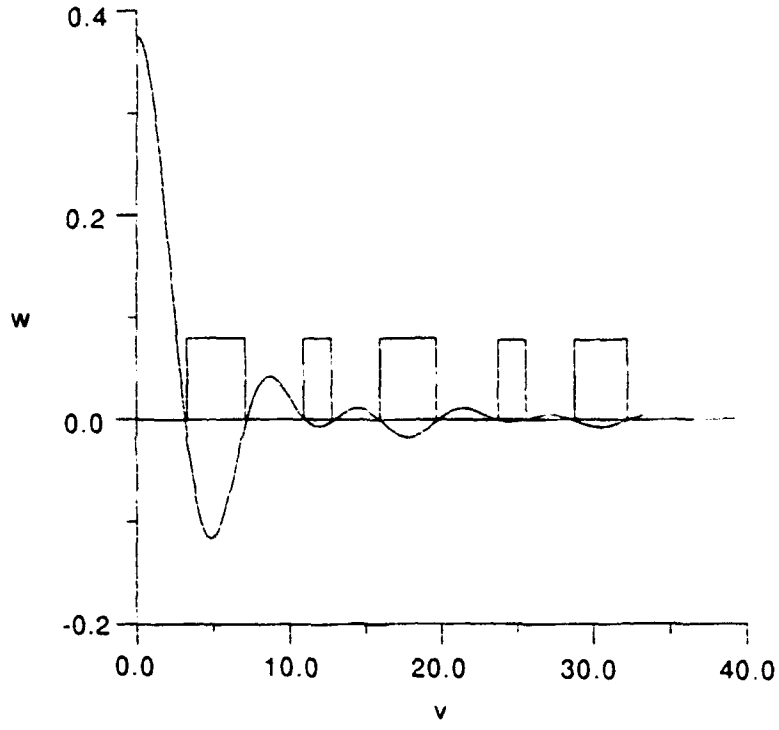

Figure 7
Matched filter design for a microlens size of ten times the Airy spot size.

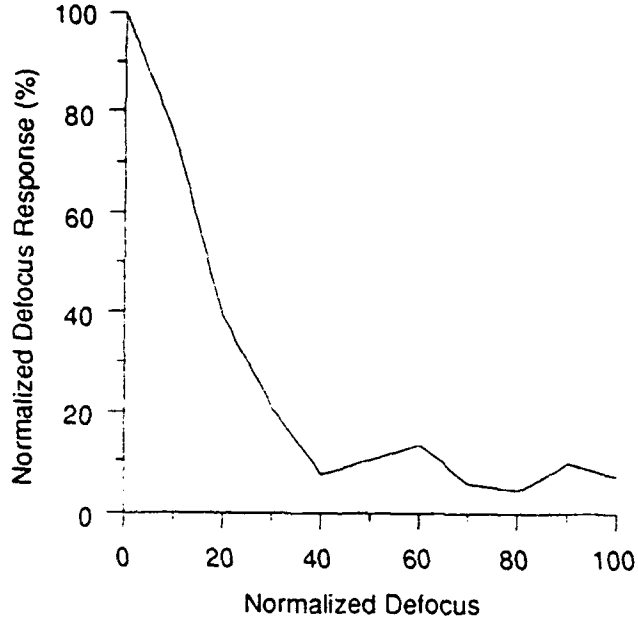

Figure 8
Defocus response for a pixel filter in which the wavefront matched filter includes two rings.

3.0 ABERRATION EFFECTS

The effects of the imaging lens were evaluated. We added a spherical aberration factor into Eq. (3) and expressed the field diffraction by the imaging lens by

$$w(u,v) = \int_{b/a}^{1} J_0(v \cdot \rho) \exp\left(j u \frac{\rho^2}{2}\right) \exp\left(j 2 \pi g \rho^4\right) \rho \, d\rho \quad . \qquad (10)$$

where g is the spherical aberration coefficient (g = 1 corresponds to one wave of spherical aberration). Figure 9 shows the defocus response curves for various values of g. They indicate that a spherical aberration smaller than $\lambda/4$ does not significantly degrade defocus response. When g is greater than $\lambda/4$, however, depth discrimination contrast is significantly degraded. The calculations above did not employ wavefront matched filters.

When using wavefront matched filters, the effect is even worse. Figures 10(a) and (b) are for the spherical aberration coefficient g = 0 and g = 1, respectively. They show that the depth discrimination capability is significantly degraded by the aberration.

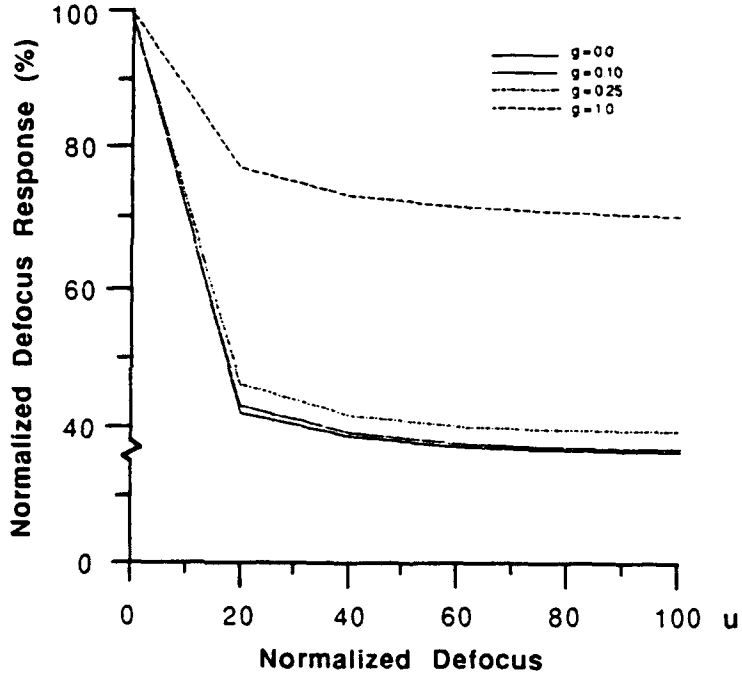

Figure 9
The aberration effects on the defocus response (without use of wavefront matched filters).

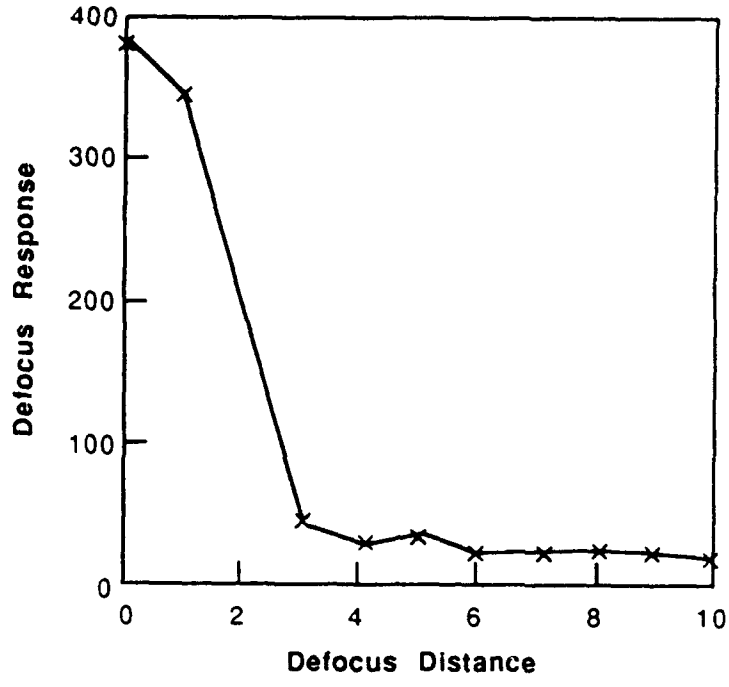

(a)

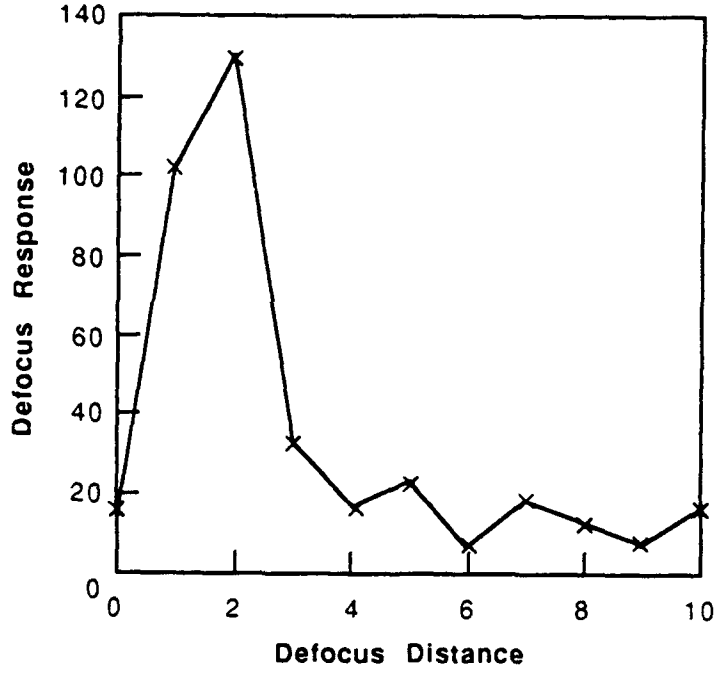

(b)

Figure 10
Aberration effects on defocus response using wavefront matched filters (a) g=0, (b) g=1.

4.0 EFFECTS OF WAVELENGTH VARIATIONS

As discussed in Section 2.0, the wavefront matched filters should match the diffraction pattern because the size of the diffraction pattern is linearly dependent on wavelength. Thus, in principle the wavefront matched filters can only match the diffraction pattern at the design wavelength. Figure 11 shows the effects of the wavefront variations on the defocus response. The curve marked "x" shows the defocus response for the design wavelength, λ_0, that with "□" is for $\lambda = 0.9\ \lambda_0$ and that with "+" $\lambda = 0.8\ \lambda_0$. They show that wavelength variation may severely deteriorate depth discrimination capability.

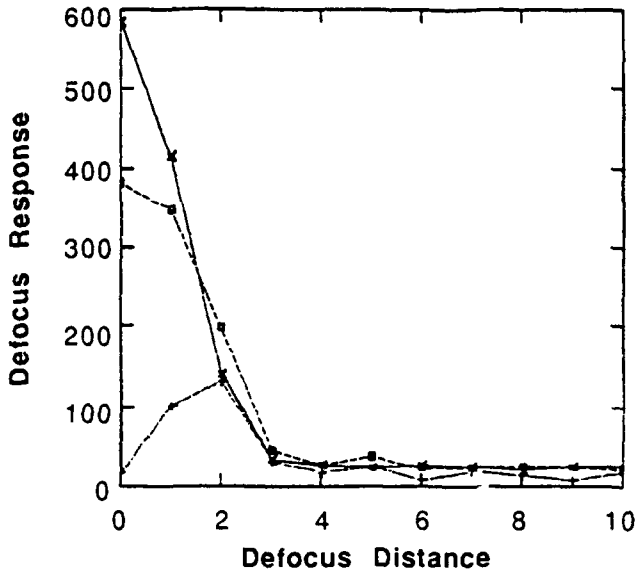

Figure 11
Wavelength variation effects on the defocus response.
"x" $\lambda = \lambda_0$ (design wavelength), "□" $\lambda = 0.90\ \lambda_0$, "+" $\lambda = 0.80\ \lambda_0$.

5.0 DEPTH DISCRIMINATION BASED ON LIGHT INTENSITY

The experimental setup is shown schematically in Figure 12. An argon laser beam passes through an aperture which filters out scattered stray light. The beam is then turned 90 degrees by a turning mirror. A beamsplitter splits the beam into two subbeams. The first subbeam is turned 90 degrees by a glass reflector on which a visible spot is formed. The spot is imaged by the imaging lens onto the CCD. The second subbeam is turned 90 degrees by a mirror and further split into two beams. One of them continues traveling to the left, and is turned 90 degrees by another glass reflector on

which a visible spot is also formed. This spot is also imaged by the imaging lens and CCD combination. After the second beam splitter, the second beam is expanded with a beam expander and is projected onto a dispersion screen, which forms a background of stray light for the two visible spots on the two glass reflectors. The computer controls the CCD camera, which registers the optical intensity of all of the pixels. The intensity of one predetermined pixel on the CCD camera is recorded, while the intensities of all the other pixels are disregarded. The CCD camera has 16 bit gray level.

During the experiment, the imaging lens/CCD camera was moved axially (as shown in Figure 12) scanning the object focal plane of the lens across the two visible spots formed by the two subbeams on the glass reflectors. These two spots are both on the optical axis. Figure 13 shows the intensity of the pixel as a function of the axial position of the imaging system. The two spots are clearly visible even though they are on the same axis and the background illumination is strong.

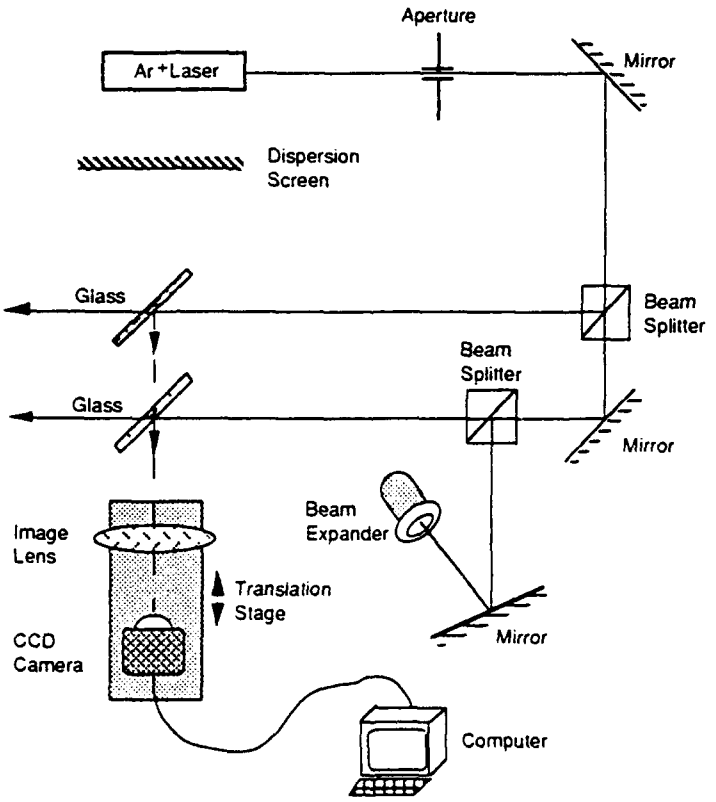

Figure 12
Setup for measuring depth discrimination based on the intensity of a single pixel of the CCD camera.

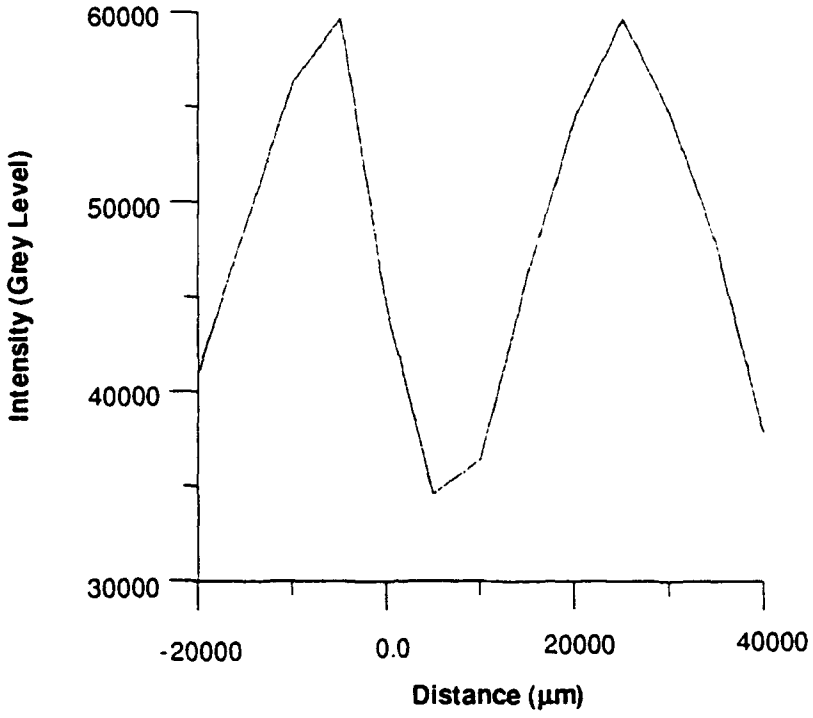

Figure 13
Intensity level versus axial position (with arbitrary zero point)
of the objective lens and CCD camera.

6.0 DEPTH DISCRIMINATION MEASURED IN THE FREQUENCY DOMAIN

The depth response of a pixel filter imaging system is depicted in Figure 14(a). We have made an observation which allows us to transform the measurement from the intensity to the frequency domain: when the system is in focus, in the neighborhood of $z = 0$, the shape of the curve in Figure 14 is approximately that of a second order polynomial. At increased defocus distances, there is a region in which the curve is approximately linear, as shown in Figure 14(a). If we modulate the defocus distance with a sine wave ($z = a \sin \omega t$), let us analyze the response at the detector. First, we consider the frequency component at 2ω. When the system is in focus, $I(z) \approx Az^2 + B$. Suppose $z = a \sin \omega t$ and the modulation amplitude a is small so that the parabolic condition is still valid. Then it follows that

$$
\begin{aligned}
I(z) &= Az^2 + B \\
&= A(a \sin \omega t)^2 + B \\
&= A[-1/2a(\cos(\omega t + \omega t) - 1)] + B \\
&= -1/2\ A \cdot a \cdot \cos(2\ \omega t) + 1/2\ A \cdot a + B.
\end{aligned}
$$

This means that when the system is in focus the detector output consists of a dc component and a component at twice the modulation frequency.

Next, let us consider the linear region in Figure 14(a), where $I(z) \approx C \cdot z + D = C \cdot a \cdot \sin \omega t + D$. The frequency component at 2ω is zero; at ω it is not zero.

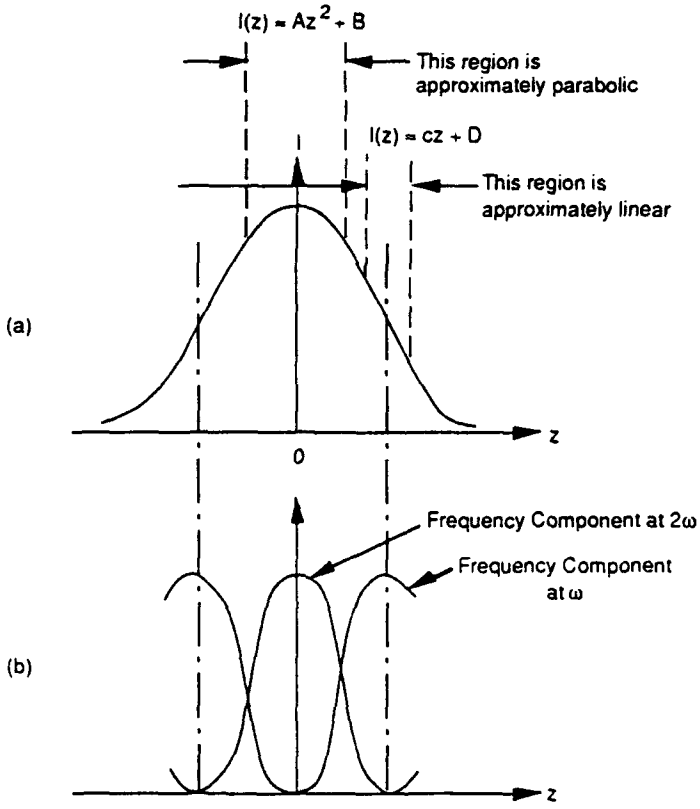

Figure 14
(a) Intensity as a function of defocus distance z. (b) Frequency components at ω and 2ω.

The frequency components at ω and 2ω are depicted in Figure 14(b). Comparing Figure 14(b) with Figure 14(a), we notice that at the defocus position z, where the second harmonic becomes

zero, the intensity curve in Figure 14(a) is still far above zero. This indicates that the 2ω curve is sharper than the intensity curve, and thus that its resolution on the z axis can be higher than that of the intensity curve.

The experimental setup for the measurement of the frequency components is shown in Figure 15. The modulation is generated by a loudspeaker, whose vibrating membrane produces a small sinusoidal displacement. A photodetector with a lens is attached to the membrane. The detector has a small active area, eliminating the need for a pinhole. A lock-in amplifier is used to amplify the frequency component while suppressing other components.

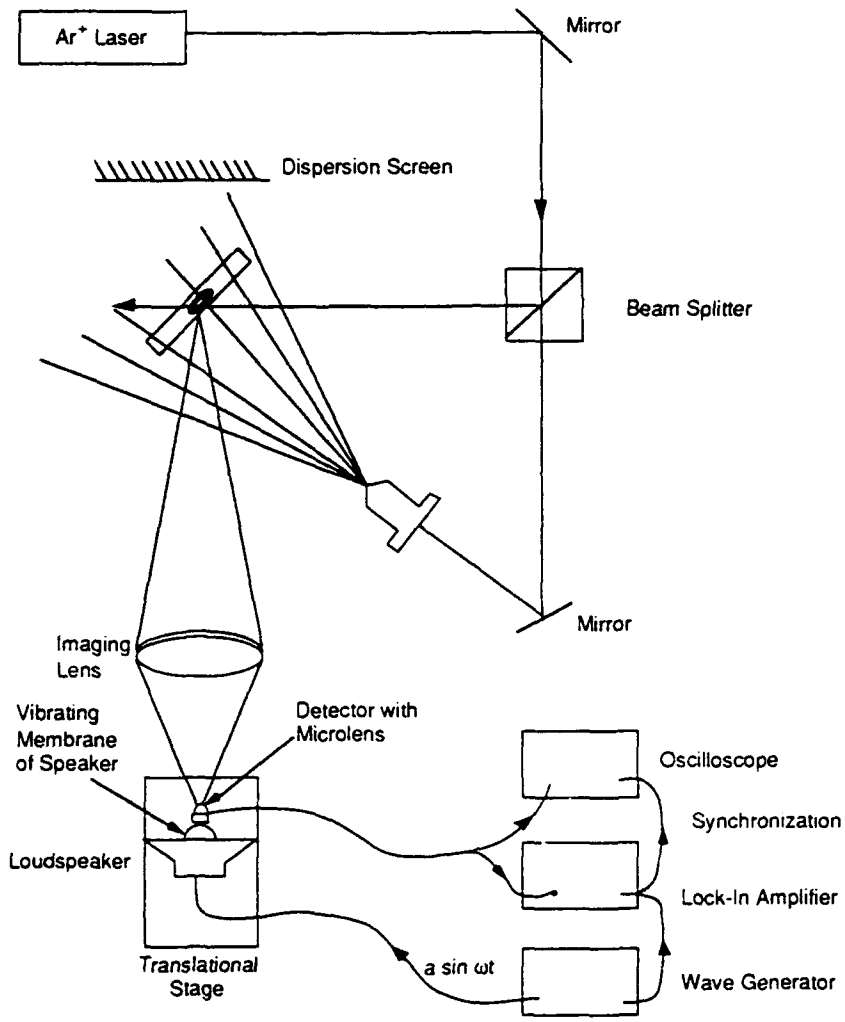

Figure 15
Experimental setup to take measurements in the frequency domain.

Results confirmed that the second harmonic indeed peaks at the in-focus position and decreases significantly outside of that position. Figure 16 shows the measured second harmonic.

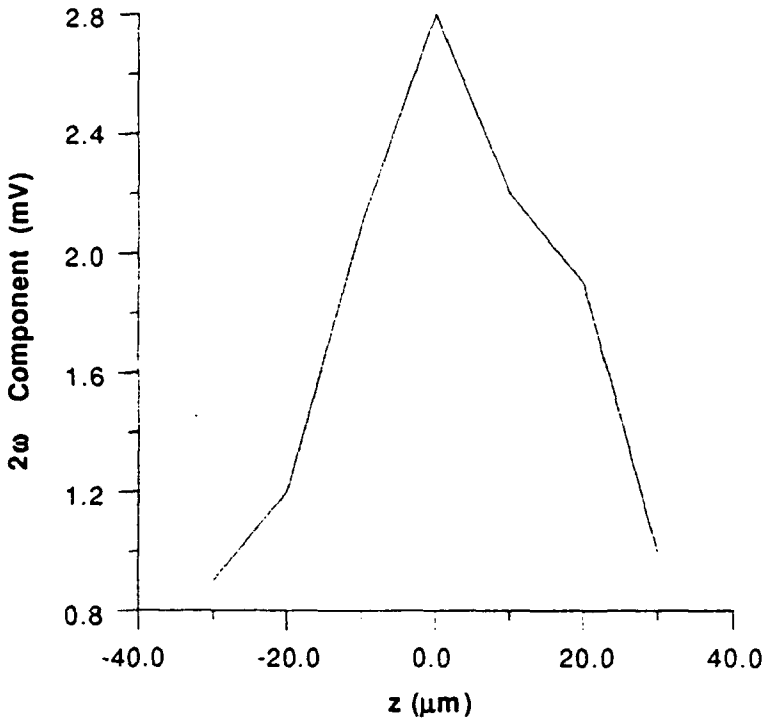

Figure 16
Amplitude of 2ω frequency components versus axial position.

The experimental setup was tuned to reduce crosstalk from the loudspeaker to the detector, caused by the strong magnetic field from the magnet in the loudspeaker. The vibration on the detector caused it to cut the magnetic flux lines from the speaker, generating a current. To reduce the crosstalk, we twisted the wires connecting the detector in order to reduce the effective magnetic flux enclosed by the wires. Electric shielding was also applied. Detector alignment was adjusted to ensure that the direction of the vibration lies on the optical axis.

7.0 PHASE II APPROACH

An immediate application of the proposed technique as identified by the Office of Naval Research is to underwater line-scan measurement, which is currently performed as shown in Figure 17.

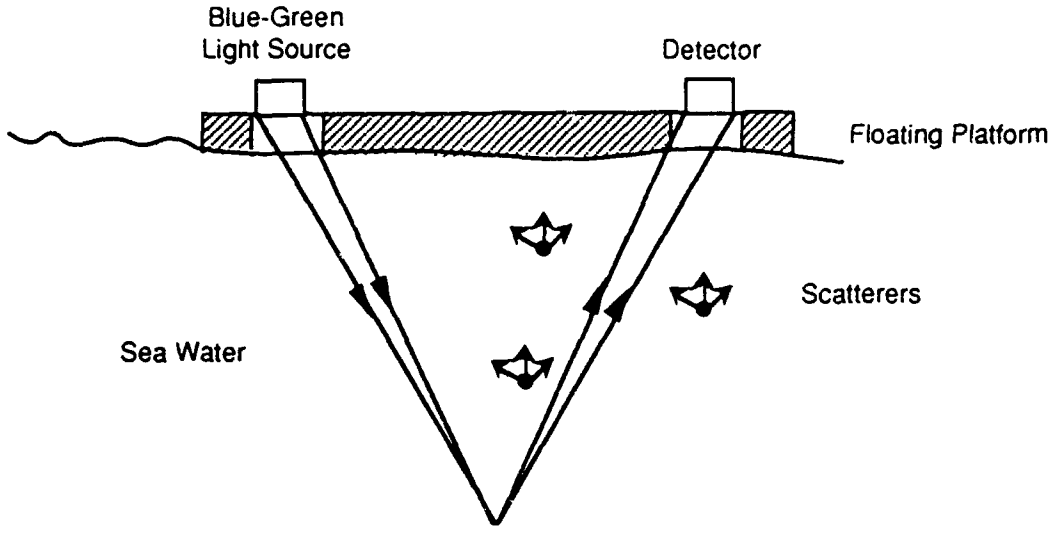

Figure 17
Current line-scan underwater measurement setup.

By simultaneously focusing both the illumination and the detector lens at the depth of interest, the system will determine the scattering characteristics of the water at just that depth. Although the received signal will include noise produced by scattering at all levels under the platform (Figure 17), the proposed pixel filtering technique will significantly increase the depth discrimination capability of the line-scan measurement, improving its signal-to-noise ratio by rejecting out-of-focus light.

8.0 CONCLUSION

During the course of Phase I, we first analytically and numerically evaluated the depth discrimination of the pixel filter. These studies indicated that pixel filters have good depth discrimination capability for an array of discrete point light sources. In particular, the wavefront-matched filter has a dramatic effect on the defocus response -- numerical simulations showed that a discrimination contrast of 20:1 is feasible. When the wavefront-matched filter is removed from the

pixel filter, the discrimination ratio becomes 5:1, which is still a significant improvement over traditional imaging optics without the pixel filter.

Subsequently, we carried out measurements to experimentally evaluate the pixel filter concept. The pixel filter used in the experiments does not contain a wavefront-matched filter, because the filter has not yet been successfully fabricated. However, we were still able to demonstrate the pixel filter's discrimination capability for discrete point sources. Two different measurement methods were employed. The first measured the light intensity at the point detector of the pixel filter as a function of defocus response. In the second method, the position of the point detector was modulated with a sine wave, and we measured the frequency components at double the frequency of the sine wave. Such a modulated measurement can yield a higher resolution in the defocus response. Both methods confirmed the discrimination capability of the pixel filter for discrete point sources.

Theoretical and experimental results have demonstrated the feasibility of the pixel filter. When the wavefront-matched filter becomes available, the defocus discrimination can be enhanced significantly.

To prepare for commercialization, POC discussed with tractor manufacturer John Deere the industrial applications of this 3-D measurement technique. John Deere needs a dynamic 3-dimensional deformation measurement instrument, and POC is considering proposing and developing a system for their application.

The pixel filter's axial discrimination capability has many potential applications for 3-D imaging instruments. These include automatic inspection and quality control, vision systems for automated circuit board inspection, and profiling and topography systems. POC has discussed applications with a variety of potential end users: 3-D autobody profiling systems (Ford Motor Company, John Deere, and Norton Equipment Corp.), tread thickness profiling (Systronics), and on-line detection of defects in extrusions and other continuous processes (Trienco, Sira, and others). Other potential applications include 3-D video systems with the added capability of distance measurement. The pixel filter can also be competitively adapted to a wide range of automated and semi-automated machine vision inspection and measurement tools. We will continue to explore the field during Phase II, selecting those applications with the greatest potential for early commercialization.